

An energetic approach to the wear behaviour of plasma-sprayed alumina–13% titania coatings

A. Rico, M.A. Garrido, E. Otero, J. Rodríguez *

Departamento de Ciencia e Ingeniería de Materiales, Universidad Rey Juan Carlos, 28933 Móstoles, Madrid, Spain

Received 28 December 2009; received in revised form 29 June 2010; accepted 1 July 2010

Available online 31 July 2010

Abstract

The wear behaviour of plasma-sprayed Al_2O_3 –13% TiO_2 coatings was determined by pin-on-disc tests that were performed at different normal loads. Conventional coatings, deposited from micrometric powders, and modified coatings, deposited using agglomerates of nanoparticles as feeding powders, were studied. The wear rates of conventional and modified coatings were compared, and the influence of the microstructure was analysed by using an energetic approach to the wear. The enhanced properties of the modified coating were justified in terms of its microstructure. It is likely that the partially melted zones in this coating were responsible for the improvement in the wear resistance via their reinforcement of the ceramic matrix composite.

© 2010 Acta Materialia Inc. Published by Elsevier Ltd. All rights reserved.

Keywords: Ceramic coatings; Plasma spraying; Wear; Nanostructure

1. Introduction

Ceramic coatings are used in tribological applications because of their favourable combination of properties: low density, hardness and chemical inertness. Coatings that are based on alumina are a good alternative when wear resistance is the limiting factor. However, the main drawback to using alumina-based coatings is their brittleness [1–3]. In order to increase the toughness of a coating, different quantities of other ceramics can be blended with alumina to maintain a balanced equilibrium between properties. Titanium oxide has a low melting point and plays a role in binding the alumina grains. Coatings of higher density with suitable hardness and increased toughness can be achieved through the blending of ceramic materials and alumina [4–6].

Alumina–titania coatings are usually manufactured by atmospheric plasma spraying. Under the high temperatures involved, coatings with a good adherence to the substrate and a limited level of porosity can be produced. The influ-

ence of the projection parameters on porosity, hardness, Young's modulus and wear resistance has been extensively studied in the alumina–titania system [1,6,7].

Following the growing interest in nanomaterials [7–14], modified plasma-sprayed alumina–titania coatings have also been prepared from nanocrystalline powders. Two main difficulties are encountered during the manufacture of the coatings: the small size of the nanoparticles impedes their direct projection in conventional plasma equipment, and the elevated temperatures that are presumably reached in the plasma may destroy the original nanostructure during thermal spraying if the process is not carefully controlled [7,9].

A new technological process was developed for preparing agglomerates of nanoparticles by spray-drying [15]. The average sizes of the agglomerates are similar to those of conventional powders (approximately 30–50 μm). These agglomerates can be projected using standard plasma equipment. The nanostructure can be maintained if the temperature during plasma spraying is held at an intermediate value between the melting points of alumina and titania [7–14].

* Corresponding author.

E-mail address: jesus.rodriguez.perez@urjc.es (J. Rodríguez).

Recently, the mechanical properties and the wear behaviour of the modified alumina–13% titania coatings have been studied [16–18]. Although a better wear resistance was reported, these studies did not use a systematic approach toward understanding the wear mechanisms, the variables and the parameters controlling the wear process.

Wear behaviour is not an intrinsic material property due to its dependency on the properties of the materials that are making contact (microstructure, roughness, grain size, mechanical properties) and with the conditions under which tests are performed (contact geometry, normal pressure, temperature, sliding velocity). There are many articles on the topic of the wear of ceramics, and several wear models have been proposed that describe the characteristic brittle fracture mechanism. The efforts of Evans, Hsu, Ashby, Kato and their colleagues must be recognized [19–36]. Hsu and Shen [37] pointed out that most of these models were developed for specific pairs of materials under defined operating conditions, and it is difficult to apply these models to other systems.

In this work, a comparison of the tribological behaviour of conventional and modified alumina–13% titania coatings was carried out under different normal pressures. Two coatings were produced based on micro-sized and nano-sized feedstock; these coatings had the same composition but different microstructural features. We investigated the link between the microstructure and the local mechanical properties, the global effective properties and the wear response.

2. Materials and experimental techniques

2.1. Materials

Al₂O₃–13% TiO₂ coatings that were deposited on SAE-1042 steel by atmospheric plasma spray (APS) were studied. Conventional coatings were fabricated from commercial powder (METCO 130 provided by SULTZER METCO™). The average particle diameter was approximately 50 μm.

Modified Al₂O₃–13% TiO₂ coatings were prepared from agglomerates that were supplied by INFRAMAT ADVANCED MATERIALS™. The original material was developed by Gell et al. [9–11] and is under a patent by INFRAMAT ADVANCED MATERIALS. The agglomerates were manufactured by spray-drying nanometric particles (Nanox™ S2613S) with an average size of 200 nm. Small additions of ZrO₂ and CeO₂ were included in order to improve the flow of the powder in the plasma and to increase the adhesion of the coating. The agglomerates, which had an average size of 30 μm, can be projected with standard APS equipment.

A Ni–Al–Mo 90/5/5 (wt.%) bond coat was deposited between the substrate and the ceramic coating to improve the adhesion. The final thickness of the coating was approximately 500 μm, including the bond coat. The parameters controlling the APS process are included in Table 1.

Table 1

Projection parameters used to deposit alumina–titania coatings and Ni/Al/Mo bond coat.

Parameter/material	Bond coat	Ceramic coatings
Current (A)	120	150
Voltage (V)	80	100
Working gas flow, Ar (SCFH)	40	40
Projection distance (mm)	120	120
Feed powder rate (g min ⁻¹)	90	80
Incident angle (°)	90	90
CPSP (A·V/SCFH)	–	375

2.2. Experimental techniques

2.2.1. Microstructural characterization

To perform a microstructural analysis, several samples were cross-sectioned using a diamond disc and metallographically prepared. The samples were analysed by scanning electron microscopy (SEM) using the Philips XL30 and JEOL 6400 microscopes. The microscopes were equipped for energy dispersive X-ray microanalysis. To determine the morphology and the composition of nanoparticles and agglomerates, some samples were prepared for analysis with transmission electron microscopy (TEM) in an FEI Tecnai 20 operating at 200 kV.

2.2.2. Mechanical characterization

Samples were prepared in plan view from the as-sprayed coatings. The samples were cut with a diamond saw and polished using 1200 grit SiC paper. These steps were followed by a subsequent polishing in a diamond slurry up to a 0.25 μm finish. Time and pressure was carefully controlled in order to minimize any artificial increase in the surface porosity or the excessive removal of poorly bonded regions. Finally, the polished surfaces were cleaned in deionized water, and were then cleaned by ultrasonication in propanol.

Depth-sensing indentation tests were carried out using a diamond Berkovich indenter with a nominal edge radius of 100 nm. The experimental device was a Nanoindenter XP (MTS System Co.) equipped with a high load modulus. The nanoindenter applies a load via a calibrated electromagnetic coil with a resolution of 50 nN. The displacement of the indenter was measured using a capacitive transducer with a resolution of 0.01 nm. To differentiate the values of Young's modulus and the hardness of the microstructural constituents, a matrix of 204 (17 × 12) indentations was made inside a representative area using a maximum load of 200 mN. The distance between the indentations was set at 5 μm. The Oliver and Pharr method was used to analyse the load-depth of the penetration curves and to obtain the Young's modulus and the hardness for each location of indentation [38].

A similar approach was used with the indentation fracture toughness, K_{IC} . A matrix of indentations (10 × 15) was made on a representative area of the sample. A maximum load of 1 N was applied, which is large enough to induce

fracture around the imprint. The distance between the indentations was maintained at 20 μm . The usual procedure for determining the indentation fracture toughness [39] cannot be applied unless a regular crack pattern is developed. Unfortunately, a regular crack pattern did not develop with the modified and conventional samples. Therefore, the indentation fracture toughness was calculated by following the method described in Ref. [40]. The coating failure is associated with pop-in events that appear as discontinuities in the loading curve. The fracture dissipated energy, U_{fr} , can be derived from the difference between the experimental curve and the hypothetical curve that is obtained in the absence of failure. After the indentation tests, the fractured area, A_{fr} , around the residual imprints was measured with SEM. Finally, the indentation fracture toughness, K_{IC} , of the coating was calculated using the following equation:

$$K_{\text{IC}} = \left[\frac{EU_{\text{fr}}}{(1 - \nu^2)A_{\text{fr}}} \right]^{\frac{1}{2}} \quad (1)$$

E and ν are the Young's modulus and Poisson's ratio of the coating, respectively. A Poisson's ratio of 0.28 was used for all coatings.

2.2.3. Wear tests

Wear tests were carried out in a wear-testing machine (WAZAU TRM 1000) with a pin-on-disc configuration under dry sliding conditions and without eliminating the formed debris. Before the test, the specimen and the counterbody were cleaned using methanol in order to avoid the presence of humidity and other undesirable films such as grease. The average sample roughness was always kept in the range $10 \pm 3 \mu\text{m}$. Most of the procedures for the ASTM standard G99-04 were followed [41]. However, several modifications were introduced that primarily involved the pin shape. Prismatic pins were made of the material under study (with modified and with conventional coatings) with a rectangular section of $2.5 \text{ mm} \times 6.3 \text{ mm}$. With this geometry, the nominal contact area remained constant during the tests despite the wear process. The disc was made to have the same coating as the sample and all the wear test conditions were selected according to the industrial application in which this material is involved. The disc rotates horizontally at a sliding speed of 0.1 m s^{-1} . A dead-weight loading system was used to perform the tests at nominal normal pressures ranging from 5 to 65 MPa. At least three tests were carried out at for each experimental condition. The coefficient of friction was obtained using a torque transducer and the variation of the pin height was registered using a linear variable differential transformer with a precision of $\pm 1 \mu\text{m}$. The pin wear rate was calculated through mass measurements using a METTLER–TOLEDO balance with a resolution of 0.01 mg. The wear rate was computed using the following equation:

$$k = \frac{\Delta m}{\rho FL} \cdot 10^{-6} \quad (2)$$

where Δm is the mass loss of the pin, ρ is the coating density (3970 kg m^{-3} for both coatings), F is the normal load and L is the sliding distance.

Finally, the worn specimens were cross-sectioned using a microcutter (Struers Accutom-5). In order to analyse the microstructural changes in the nearest zone at the pin contact surface, plane- and cross-sections of the worn surfaces were prepared with conventional metallographic techniques and observed with the help of scanning electron microscopes (Philips XL 30 and Hitachi S4400). The debris morphology and size were also examined with SEM.

3. Results

3.1. Microstructure

The agglomerates of nanoparticles that were obtained after spray-drying were used as feeding powders for the deposition of the modified coatings. The agglomerates exhibited a spherical shape, with an average diameter of about $30 \mu\text{m}$ (Fig. 1a). They were themselves formed by irregularly shaped, polygonal nanoparticles. The TEM study that was performed on the agglomerates revealed that they were composed of $\gamma\text{-Al}_2\text{O}_3$ (Fig. 1b) and anatase- TiO_2 (Fig. 1c). Generally, the anatase particles were the smallest, ranging from 50 to 70 nm, while the $\gamma\text{-Al}_2\text{O}_3$ particles were approximately 200 nm.

Fig. 2 shows the hierarchical microstructure that was exhibited by the modified coating. The main microstructural details of the conventional coating are also included for comparison. The relevant microstructural features have been quantified. In Fig. 2a, the cross-section of the modified coating is shown. Three layers were observed. The upper layer is the ceramic coating. The intermediate layer corresponds to a Ni/Al/Mo bond coat that was used in order to minimize the residual stresses that occur due to the mismatch between the thermal expansion coefficients of the metallic substrate and the ceramic material. The substrate was made of SAE-1042 carbon steel. To retain the original nanostructure, the projection parameters should be selected and controlled in order to fix the temperature of the plasma between the melting temperatures of both components ($\gamma\text{-Al}_2\text{O}_3$ and TiO_2). Fig. 2b and c shows details of the modified coatings and the conventional coatings, respectively. Both of the coatings had a common microstructure. The microstructure consisted of splats that were formed by the deposition of individual molten droplets; these splats generated a lamellar, fully melted structure (FM) that is typically obtained when thermal projection techniques are used. The typical defects of APS coatings also appear in the studied materials. For example, the pores and vertical contraction cracks can be easily found in Fig. 2a and b. In the literatures [3–8], TEM studies of similar coatings indicated that the FM phases are primarily composed of nanocrystallites of $\gamma\text{-Al}_2\text{O}_3$. However, at this scale, a difference was observed in the modified coating. Spherical partially melted (PM) zones, including nanoparticles, were

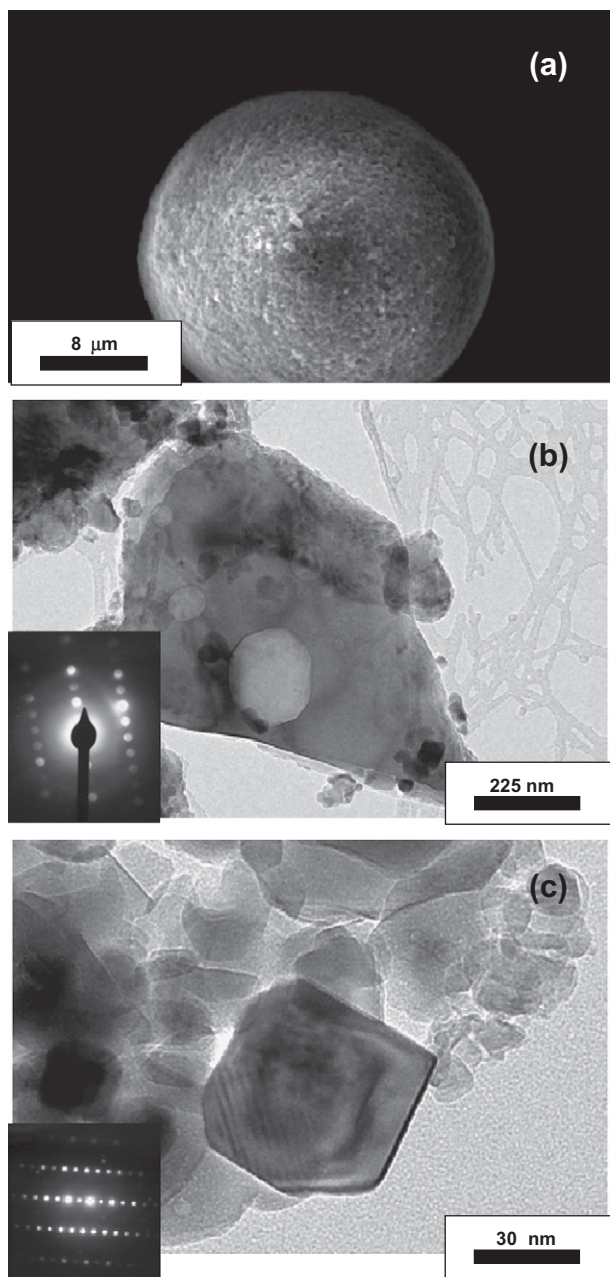


Fig. 1. (a) Panoramic view of the agglomerate used as feeding powder in the deposition of the modified coating. (b) TEM image of a γ -alumina nanoparticle showing an electron diffraction pattern (EDP) with B (1 2 3) orientation. (c) TEM image of an anatase-TiO₂ particle showing an EDP with B (2 1 0) orientation.

also observed in the modified coating due to the deposition of semi-molten droplets. These microstructural features could not be found in the conventional system. The PM zones exhibited a composite microstructure, as shown in the TEM image in Fig. 2d. The observed nanoparticles had an average size of 200 nm and corresponded to the alumina particles that were previously identified in the feeding powders. However, the electron diffraction pattern indicated that a phase transition occurred during the plasma projection. The PM zones were essentially composed of α -Al₂O₃, while

the main phase in the powder was γ -Al₂O₃. Although the particles maintained their initial size, they lost the polygonal contour and displayed a smooth and round final shape. The high temperatures reached during the projection promoted the phase transition, but the temperatures were not high enough to completely melt the particles. The α -Al₂O₃ nanoparticles were then embedded in a matrix that was composed of γ -Al₂O₃ nanocrystallites that were similar to those presented in the FM zones. The only difference with the FM domains was that the γ -Al₂O₃ matrix was supersaturated with Ti⁴⁺ because of the formation of a solid solution between the γ -Al₂O₃ and the TiO₂. These results are in agreement with those obtained elsewhere [3,5,7]. Thus, the modified coating presents a multiphase microstructure with several levels in a hierarchical system. In fact, the microstructure resembles a ceramic composite in which the matrix is mainly composed of nanocrystallites of γ -Al₂O₃ (FM zones). The reinforcement particles (PM zones) are composed of α -Al₂O₃ nanoparticles embedded in a γ -Al₂O₃ matrix.

3.2. Mechanical characterization

We used depth-sensing indentation tests to determine the mechanical properties of the coatings on a local scale in order to distinguish the behaviour of each of the microstructural constituents. These tests were performed to determine the effective properties of the coatings.

3.2.1. Young's modulus and hardness

Young's modulus and hardness have been investigated in previous studies [16]. A statistical analysis was performed using data from the indentation matrix that was carried out on the modified and conventional samples. Fig. 3 shows the resultant histograms of the Young's modulus and the hardness from the modified coating. Several distributions are easily identified: the first distribution corresponds to the FM regions and the second distribution is associated with the PM particles. A third set of data were associated with the indentations that were made on pores and cracks. The experimental results yield some important observations:

- The depth-sensing indentation tests were able to discriminate between different microstructural regions of the modified coating.
- The PM particles were stiffer and harder than the FM regions. The increased stiffness and hardness are likely due to the presence of α -alumina nanoparticles inside the PM particles. In addition, the FM domains were mechanically indistinguishable from the conventional coating.
- The experiments were sensitive to material defects such as pores and cracks.

To estimate the effective mechanical properties of the modified coating, a simple rule of mixtures was used. The volume fraction of PM domains, V_f^{PM} , was measured via optical microscopy and was found to be $\sim 30\%$. The

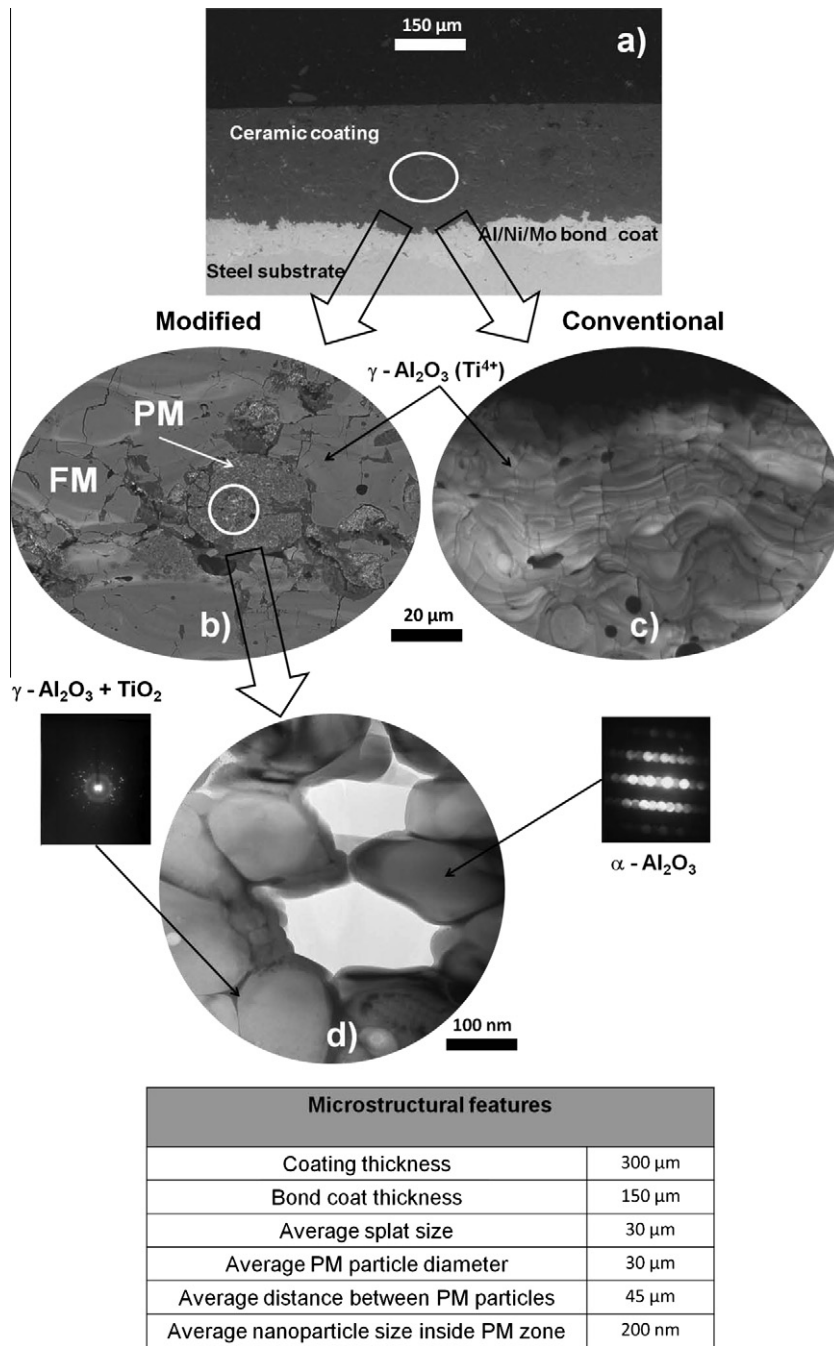


Fig. 2. Schematic representation of the hierarchical microstructure in the coatings. (a) Panoramic view of the coating system. (b) Cross-section of the modified coating showing a partially melted zone embedded in a fully melted region. (c) Cross-section of the conventional coating showing the typical APS coating's splat morphology. (d) TEM image showing the morphology and composition of nanoparticles inside the partially melted zone from the modified coating. An EDP corresponding to an $\alpha\text{-Al}_2\text{O}_3$ nanoparticle with a B (1 1 1) orientation and an EDP corresponding to the surrounding matrix are also presented.

Young's modulus and the hardness of the FM matrix and the PM reinforcement were obtained from the data presented in Fig. 3. Table 2 outlines the main results of these tests.

3.2.2. Indentation fracture toughness

A similar statistical analysis was carried out using that fracture toughness values that were measured from the

matrix of indentations performed on the coatings. The fracture toughness histogram is presented in Fig. 4. Two distributions were exhibited by the modified coating, but a wide, single distribution was observed for the conventional material. The PM domains appeared to be tougher than the FM regions in the modified coating. Interestingly, the fracture toughness that was measured in the FM regions was also higher than the conventional coating.

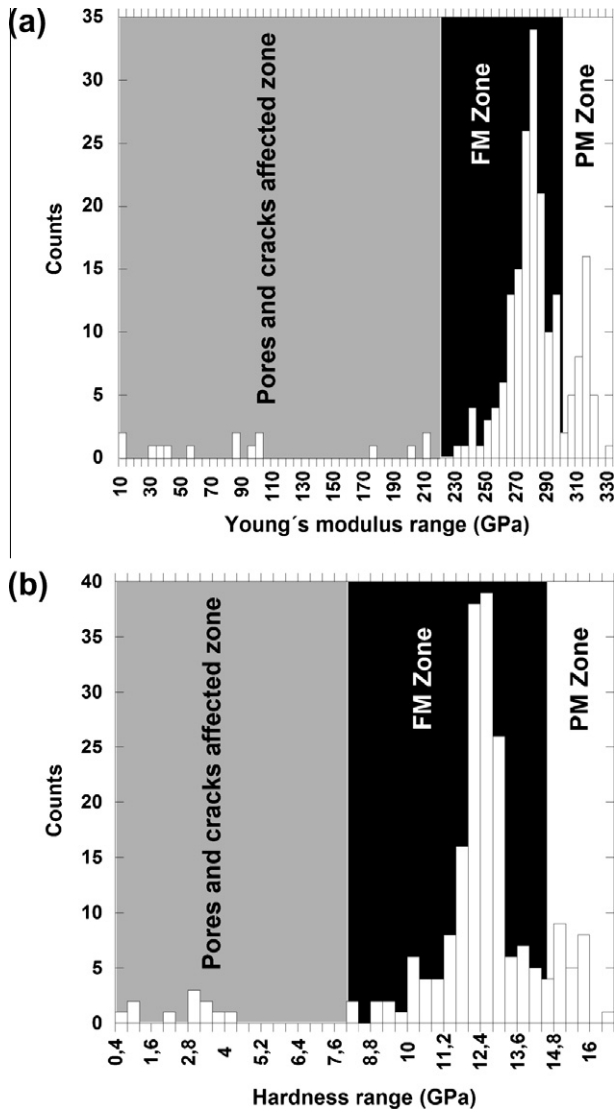


Fig. 3. Statistical distribution for the mechanical properties of the modified coating obtained from depth-sensing indentation analysis. (a) Young's modulus. (b) Hardness.

Rose suggested a model to estimate the effective fracture toughness for a composite made of a brittle matrix that is reinforced by well-bonded particles [42]. This description generally applies to the material studied here. In terms of the modified coating parameters, the model can be written as:

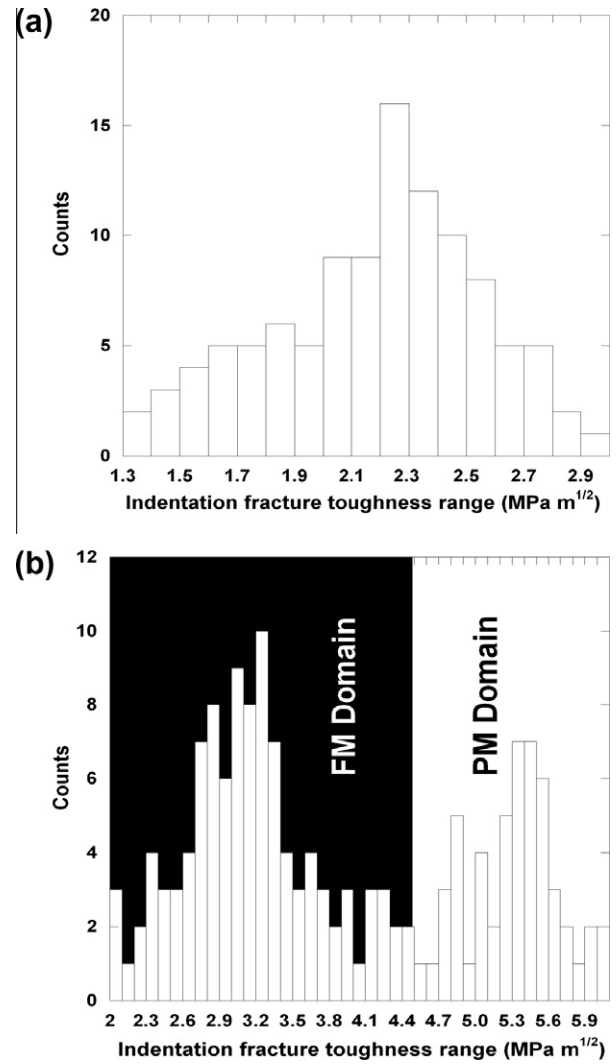


Fig. 4. Statistical distribution for the indentation fracture toughness of the coatings, obtained from depth-sensing indentation analysis. (a) Conventional. (b) Modified.

$$K_c^{MOD} = K_c^{FM} \sqrt{\left(1 - 2\frac{R}{L}\right) + 2\frac{R}{L} \left(\frac{K_c^{PM}}{K_c^{FM}}\right)^2} \quad (3)$$

where R is the particle radius, L is the centre-to-centre distance of the particles. K_c^{MOD} , K_c^{PM} and K_c^{FM} are the effective fracture toughness of the modified coating, the fracture toughness of the PM domain and the fracture toughness for the FM region, respectively. Expression (3) is a rule

Table 2
Mechanical properties of the coatings measured by means of depth-sensing indentation.

	Modified coating			Conventional coating
	PM domain	FM domain	Effective property	
Young's modulus, E (GPa)	300 ± 16	269 ± 18	278 ± 17^a	265 ± 15
Hardness (GPa)	14.0 ± 0.9	9.7 ± 1.1	11 ± 1.0^a	9.6 ± 0.7
Fracture toughness ($\text{MPa m}^{1/2}$)	5.4 ± 0.7	3.0 ± 0.8	4.8 ± 0.8^b	2.2 ± 0.8

^a Using a simple rule of mixtures.

^b Using Eq. (3).

of mixtures that was applied to the specific fracture energy, G_c . The propagation of a crack in a brittle matrix reinforced by well-bonded particles was further investigated by Bower and Ortiz [43], who used a numerical analysis to demonstrate that the Rose model fit well with the experimental data if R/L was in a range from 0 to 0.3. The ratio R/L in the modified material remained approximately in this range. Accordingly, Eq. (3) was applied in order to estimate the effective fracture toughness of the modified coating using the data from Fig. 4. A summary of the calculated results is compiled in Table 2.

3.3. Tribological behaviour

3.3.1. Wear rate and friction coefficient

Fig. 5a shows the wear rate of the coatings vs. a nominal normal pressure. The modified coating exhibited lower wear rates than the conventional coating for all of the experimental conditions. When the normal pressure was low (<15 MPa), the differences between the dissimilar coatings reached a factor close to 4. Both of the materials displayed evidence of a transition between the mild and severe wear regimes (marked with arrows in Fig. 5a), as detected by abrupt increases in the wear rate and the friction coefficient values (Fig. 5b). This transition was associated with wear rate changes of up to two orders of magnitude. The critical normal pressure at which the transition was promoted was higher in the modified coating and highlights the superior protection offered by this material relative to the conventional one. The values of the critical normal pressures were 20 and 40 MPa for the conventional and modified coatings, respectively.

The friction coefficient vs. the nominal pressure data is presented in Fig. 5b. A transition between mild and severe wear was also observed, but the critical pressure was higher for the modified coating than for the conventional one. Although the transition was delayed in the modified coating, the values corresponding to mild wear ($\mu \sim 0.5$) and severe wear ($\mu \sim 0.85$) were similar in both coatings.

3.3.2. Wear mechanisms

The transition detected in the wear rate and the friction coefficient suggests that the wear mechanism is dependent upon the nominal normal pressure. The worn surfaces of the conventional and the modified coatings that were tested at low normal pressures (5 MPa) are presented in Fig. 6. Brittle crack propagation through the splat boundaries seemed to be the operative wear mechanism in the mild wear regime. The crack propagation along the splat boundaries was especially evident in the conventional coating (Fig. 6a). However, in the modified coating, the PM zones were capable of deflecting cracks that obstructed its propagation (Fig. 6b). The role played by the PM zones is tribologically significant and could also justify the increase in the coating fracture toughness shown in Table 2.

In agreement with Williams [44], “Each of the various processes by which material can be lost from a surface in

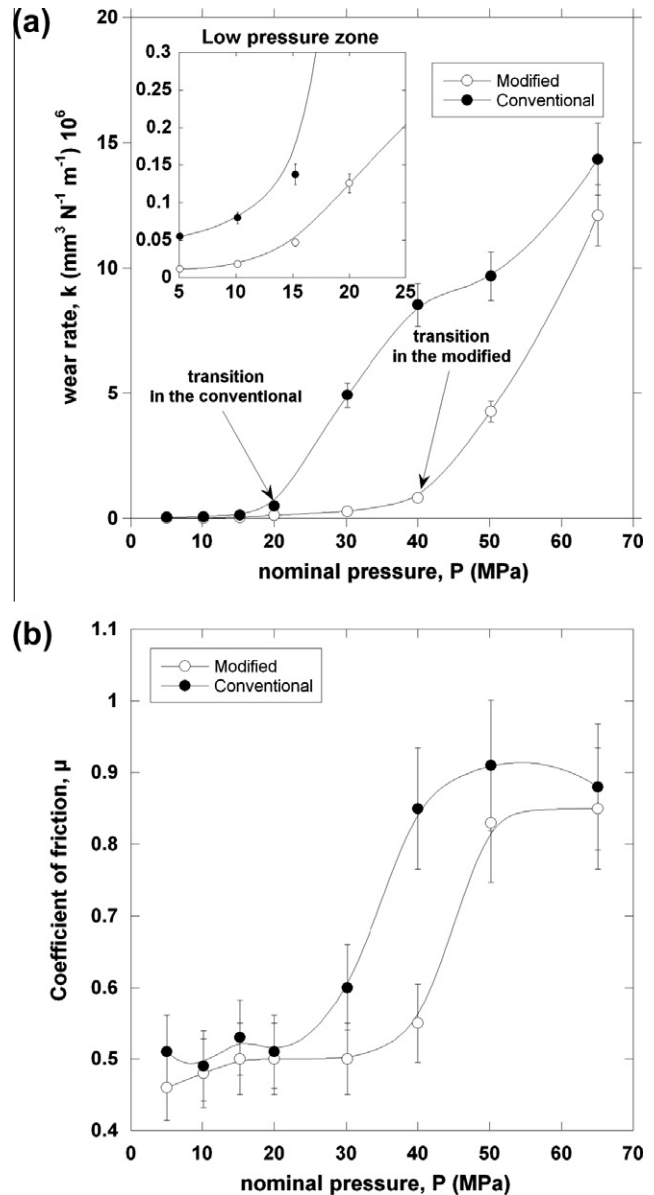


Fig. 5. Wear rate (a) and friction coefficient (b) vs. normal nominal pressure for both conventional and modified coatings.

service leaves its fingerprint both in the topography of the worn surface and in the size, shape and number of the particles which make up the wear debris”, a statistical analysis of the wear debris was performed. Fig. 7 presents an example of debris particles that were obtained from tests carried out within the mild wear regime for both the conventional (Fig. 7a) and the modified coating (Fig. 7b). There were no indications of plastic deformation. The absence of marks support the hypothesis of a mechanism that is dominated by brittle crack propagation. Fig. 7a shows a particle that was removed from the conventional coating and corresponds to a single splat extracted from the lamellar microstructure. The observation of this single splat in the debris supports the theory that crack propagation follows the splat boundaries. A debris particle from

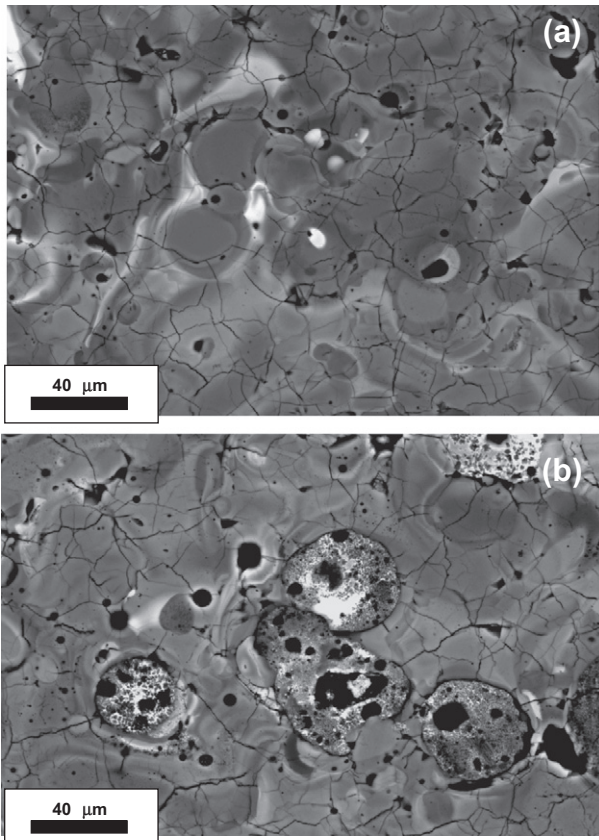


Fig. 6. SEM images showing plan views of the worn surfaces obtained from tests performed at mild wear conditions (5 MPa). (a) Conventional. (b) Modified.

the modified coating is shown in Fig. 7b. The crack deflects around the PM particle and increases the wear resistance of the material.

Histograms that show the size distribution of the debris particles obtained in the mild wear regime are presented in Fig. 8. Although a wide distribution was observed, an average value could be determined for each material. The average debris size for the conventional coating was approximately 30 μm . In the modified material, the average debris size was closer to 42 μm . The debris size values were correlated with microstructural features (see Fig. 2). In the conventional coating, the debris size was similar to the splat size. In the modified coating, it was comparable to the space between PM zones if a regular distribution was assumed.

When tests were implemented in the severe wear regime, brittle crack propagation remained the primary wear mechanism (Fig. 9); however, the crack patterns were different. Large transverse cracks crossed the splat borders in both types of coating (Fig. 9a and b). The FM/PM interfaces were also fractured in the modified coating (Fig. 9c). Cracks can easily reach the interface between the ceramic coating and the metallic bond coat, introduce damage to the material in the form of complete spallation and produce an abrupt increase in the wear rates by several orders

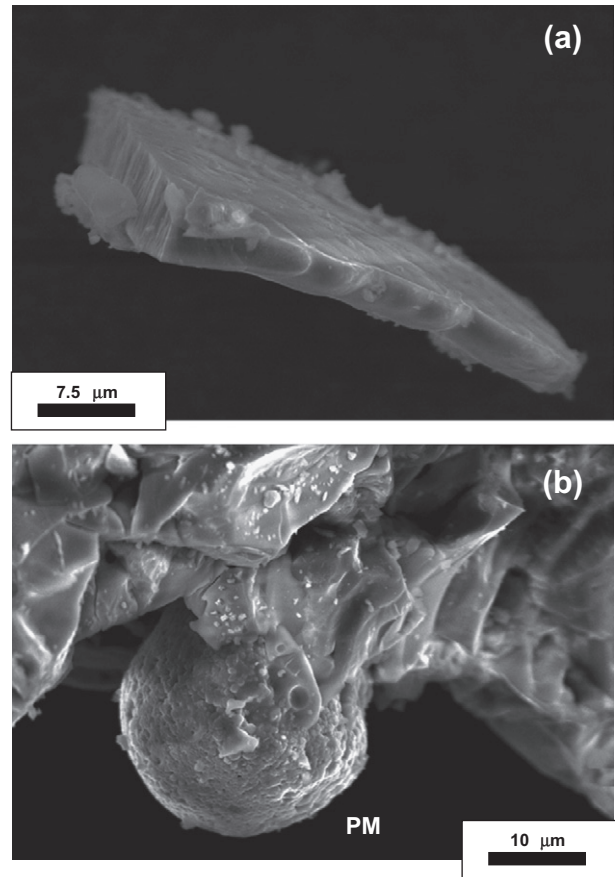


Fig. 7. SEM images showing the debris morphology obtained from mild wear conditions (5 MPa). (a) Conventional. (b) Modified.

of magnitude. The friction coefficient also exhibited a substantial increase in this regime, which may be explained by the higher roughness of the worn surfaces.

The delay in the transition from mild to severe wear in the modified material is assumed to be due to the effect of the PM particles on the crack propagation. The PM particles must postpone the activation of the trans-splat mechanism at higher nominal pressures and, when the contact severity is high enough to allow the crack to penetrate into the PM zone, a new deflection mechanism at a lower scale (200 nm) is triggered around the $\alpha\text{-Al}_2\text{O}_3$ nanoparticles (Fig. 9c). Again, this process is a consequence of the hierarchical microstructure that is formed during the thermal deposition.

The debris morphology can also be related to the wear mechanism in the severe regime. In Fig. 10a, an example of a debris particle that was removed from the conventional coating is shown. The particles are larger than those obtained from low normal pressure tests. Brittle fracture features are visible. A detail of the conventional debris particle is shown in Fig. 10b, indicating the presence of broken splats that reveal a trans-splat mechanism. Fig. 11 shows debris particles that were obtained from the modified coating that had cracks crossing the FM zones (splats) and the PM particles. The deflection mechanism around

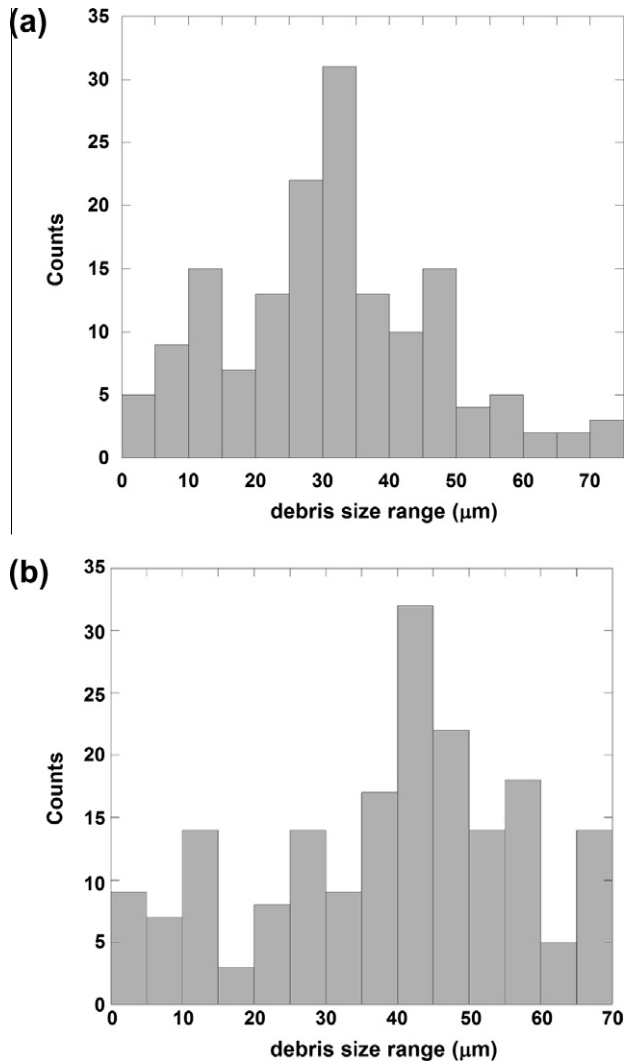


Fig. 8. Histograms showing the debris size distribution at mild wear conditions. (a) Conventional. (b) Modified.

the α - Al_2O_3 nanoparticles is also shown (Fig. 11b and c). The presence of these 200 nm particles in the PM regions not only improves its mechanical properties, but also activates wear mechanisms that do not exist in the FM zones or in the conventional material.

In Fig. 12, histograms of the debris size distribution under severe wear conditions are shown. The mean values are larger than those obtained in the mild wear regime. The mean size is larger for the modified material than for the conventional one.

4. Discussion

The wear tests revealed that brittle crack propagation is the primary wear mechanism observed, meaning that fracture toughness should be the key material property. In addition, both the modified and the conventional coatings displayed a transition between the mild and the severe wear regimes. This transition was detected by an abrupt increase

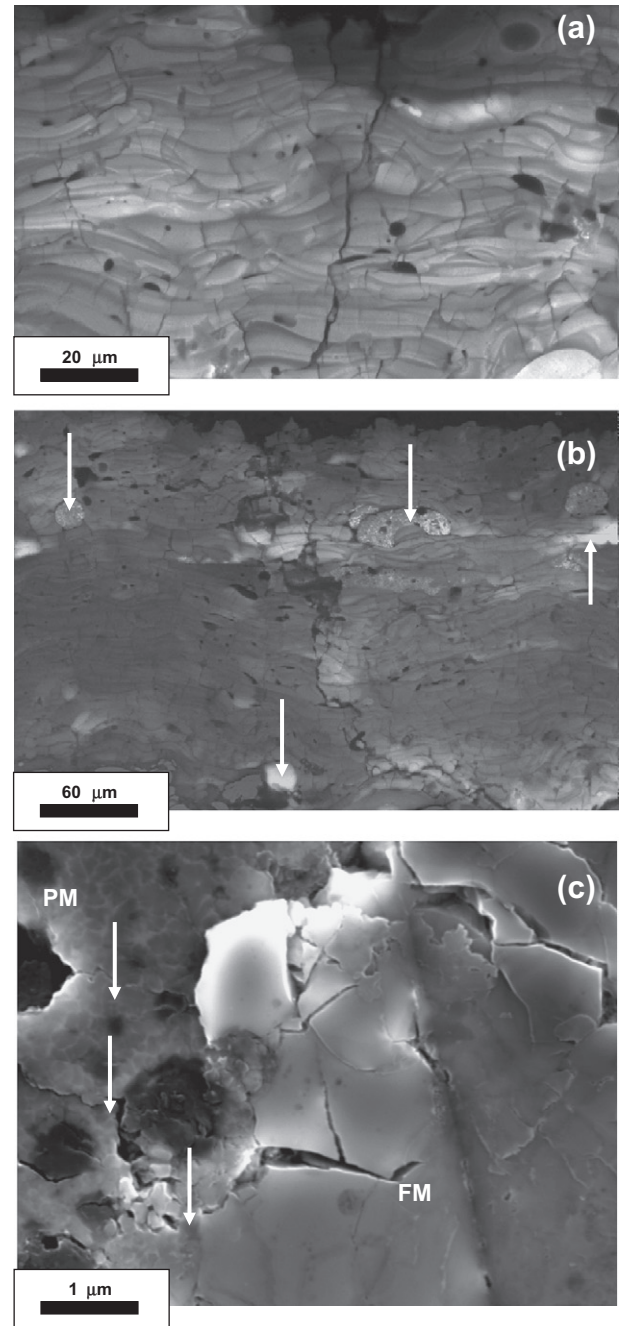


Fig. 9. SEM images showing the cross-sections of the worn surfaces obtained from tests performed at severe wear conditions (65 MPa). (a) Conventional. (b) Modified. The white arrows mark PM particles in the modified coating. (c) Detail of cracks being deflected inside a PM zone. White arrows indicate the crack paths.

of several orders of magnitude in the wear rate, an augmentation in the friction coefficient, a change in the crack path propagation and a variation of the debris size. In the mild wear regime, the cracks grow along the splat borders. In the severe wear regime, cracks transversely propagate through the ceramic layer and sometimes cross the splats and PM zones.

The analysis of the factors that affect the wear behaviour was complex. The wear resistance is not a material property,

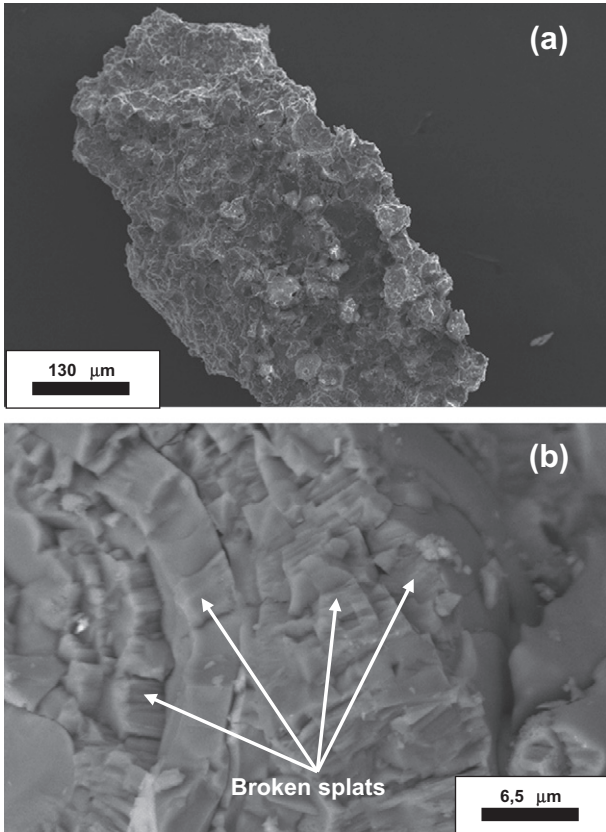


Fig. 10. SEM images showing the debris obtained from conventional coatings at severe wear conditions (65 MPa). (a) Panoramic view. (b) Detail from (a).

but it depends upon mechanical performance and operating parameters such as load, sliding velocity and temperature.

In this study, the material wear resistance was investigated by making energetic considerations. The final aim of this work was to build a wear map that uses dimensionless parameters (including material properties and working conditions) and explains why the modified coating presented better wear behaviour than the conventional one.

To describe the material wear behaviour, the dimensionless wear coefficient, kH (k is the wear rate and H the material hardness), can be written as a function, Φ , of the ratio between the input energy, I , and the energy that is dissipated by the material during the wear process, D :

$$kH = \Phi\left(\frac{I}{D}\right) \quad (4)$$

The large number of variables affecting the wear behaviour makes it difficult to determine the right form for I and D . There are several ways to establish these expressions but, among them, dimensional analysis was adequate. This methodology is based on the Buckingham theorem [45]. Every physical magnitude (i.e. the wear rate) can be correlated with a group of dimensionless ratios that comprise the physical variables that are responsible for the phenomenon (the wear, in the case of this study). The main difficulty of

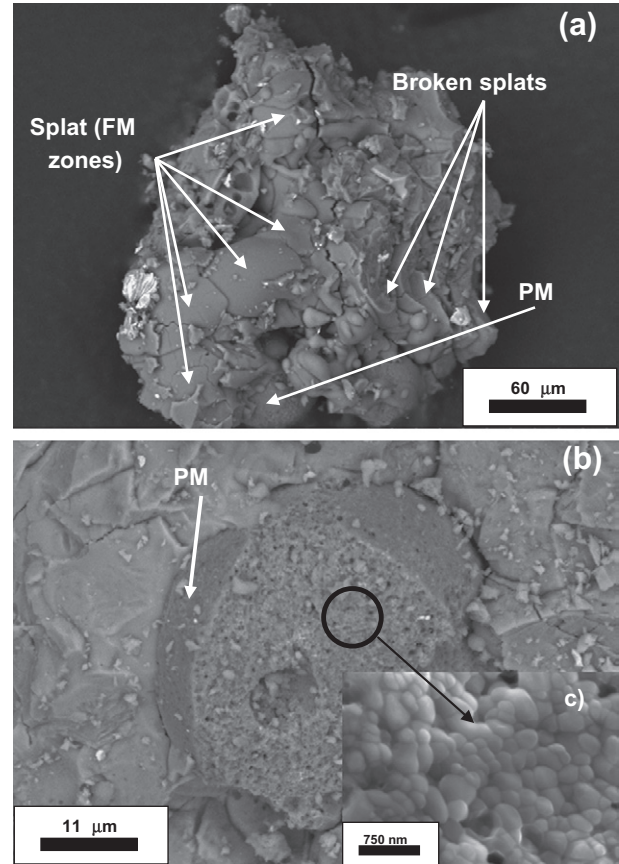


Fig. 11. SEM images showing the debris obtained from modified coatings at severe wear conditions (65 MPa). (a) Panoramic view. (b) Detail of a broken PM zone. (c) Fracture surface from the broken PM domain shown in (b).

this method lies in the fact that the parameters that influence the problem must be known a priori.

The primary wear mechanism was brittle crack propagation. Consequently, the fracture toughness, K_{IC} , hardness, H , and Young's modulus, E , were the relevant mechanical properties to explain the observed results. Because a fraction of the input energy is dissipated through frictional heating, properties like the specific heat, c_p , and the thermal conductivity, k_T , must be included in the analysis. Together with the density, ρ , the thermal diffusivity, d , comprises all of these parameters. On the other hand, the operation conditions such as normal nominal pressure, p , and the sliding velocity, v , should be considered in the analysis. Furthermore, several parameters that account for the properties of the particular contact must be added. The friction coefficient, μ , and the equivalent contact radius, r_{eq} (the square root of the nominal contact area divided by π), can be used for this purpose. Finally, a characteristic length must be included in order to satisfy the dimensional analysis requirements. The average debris size, l^* , was chosen because this parameter incorporates the values that represent each material and wear regime.

Using the Buckingham theorem [45], it is possible to write the wear coefficient, kH , as a potential function that depends upon the rest of the variables that are grouped

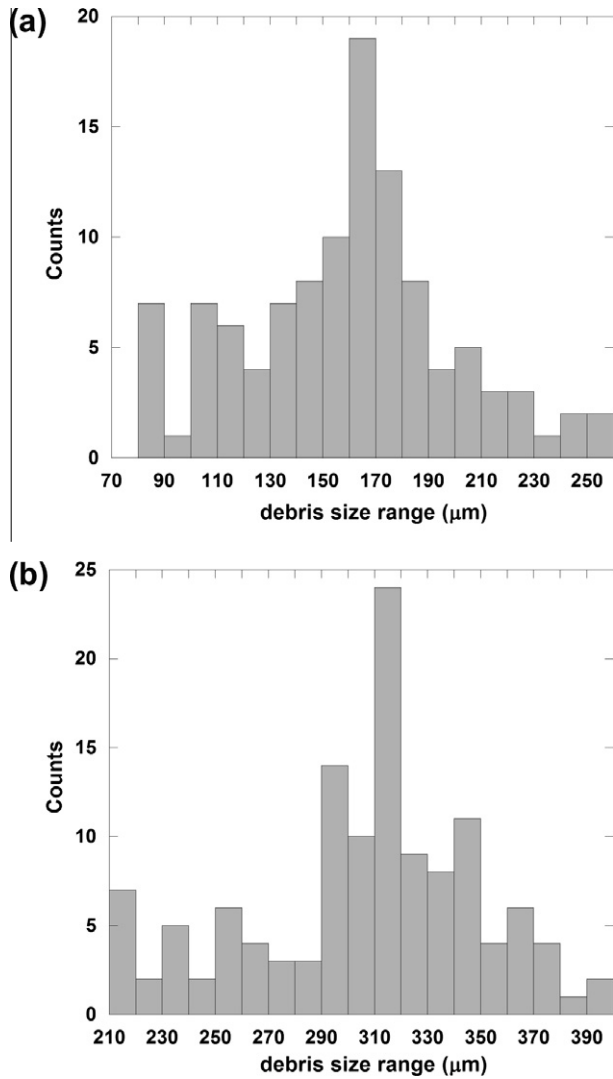


Fig. 12. Histograms showing the debris size distribution at severe wear conditions. (a) Conventional. (b) Modified.

into a series of dimensionless ratios. The solution leads to the next expression:

$$kH = C \left(\mu^{n_1} \left(\frac{P}{H} \right)^{n_2} \left(\frac{v \cdot r_{eq}}{d} \right)^{n_3} \left(\frac{E \cdot l^{*1/2}}{Kc} \right)^{n_4} \right) \quad (5)$$

The choice of the n_i exponents is arbitrary. Two approaches exist to establish the value for these exponents. The first approach consists of setting their values through the best fit of the experimental data. The second approach selects these exponents from a physical point of view. This second option allows for interpretation of the involved physical phenomenon because the relevance on the wear rate of each variable is taken into account. Proceeding in this way, the following expression was obtained:

$$kH = C \left(\frac{\mu \cdot P \cdot v \cdot r_{eq} \cdot E^2 \cdot l^*}{H \cdot d \cdot Kc^2} \right)^n = C \left(\mu \frac{P}{H} \frac{v \cdot r_{eq}}{d} \frac{E \cdot l^*}{G} \right)^n = C \left(\frac{\mu \bar{P} \bar{v}}{\bar{G}} \right)^n \quad (6)$$

where G is the energy-release rate of the material. This rate was introduced using the plane stress relationship between G and fracture toughness K_c (16):

$$G = \frac{K_c^2}{E} \quad (7)$$

\bar{G} is the dimensionless form of G defined as $\bar{G} = \frac{G}{E l^*}$. There is no reason to assume plane stress or plane strain conditions but, if the Poisson's ratio of these materials is taken into account, the differences are lower than 10%. The load and sliding velocity can be written in dimensionless form as $\bar{P} = \frac{P}{H}$ and $\bar{v} = \frac{v r_{eq}}{d}$, respectively [32].

The final form of Eq. (6) is similar to Eq. (4). The wear coefficient, kH , depends on a parameter that relates a dimensionless form of the input energy of the tribosystem, $\mu \bar{P} \bar{v}$, and the dimensionless form of the energy that is consumed during crack propagation through the material, \bar{G} . In this particular case, the primary wear mechanism is the brittle propagation of cracks, and it follows that the energy consumption is adequately expressed via \bar{G} .

The term $\left(\frac{\mu \bar{P} \bar{v}}{\bar{G}} \right)$ in Eq. (6) can be interpreted as a contact severity parameter by adopting the terminology previously used in the literature [19]. Under the same operation conditions (normal load, sliding velocity), a material with a minor contact severity should exhibit a lower wear rate as a result of its better mechanical behaviour.

One question remains for consideration. Similar contact severities should lead to similar wear coefficients if the phenomenon is controlled by the same wear mechanism. In Fig. 13, the wear coefficient, kH , is plotted for both materials vs. the dimensionless parameter $\left(\frac{\mu \bar{P} \bar{v}}{\bar{G}} \right)$. The experimental data that correspond to both materials are described by the same curve, confirming the previous argument. In addition, the wear data that correspond to the modified coating are shifted to the low severity contact values as a result of its better mechanical properties (see Table 2), while those

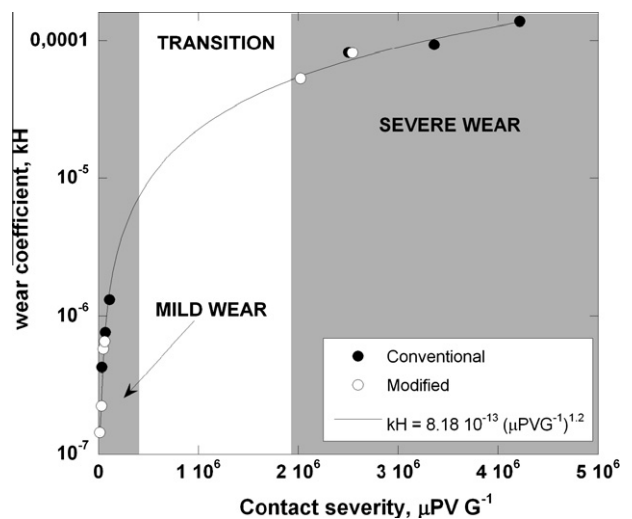


Fig. 13. Wear coefficient, kH , vs. contact severity dimensionless parameter for both modified and conventional coatings.

of the conventional coating are clearly displaced to higher contact severities. The modified coating microstructure has better effective mechanical properties (E , H and K_c), which are incorporated into the global wear parameter ($\frac{\mu P_T}{G}$). The multiphase character of the modified coating leads to lower values of this dimensionless factor.

The values of the parameters C and n in Eq. (6) are affected by all the magnitudes that are not considered in the analysis: contact geometry, surface roughness, type of movement, etc. Nevertheless, the experimental procedure (Section 2) showed that all of these testing conditions were the same for both coatings. The uniformity of the testing conditions enables the comparison shown in Fig. 13.

The main practical obstacle in the analysis presented here is that the size of the wear debris is not known before the test is performed, and this obstacle limits the prediction capability. This problem can be solved in those cases where the debris size can be related to any microstructural feature through a priori determination. This study seems to show a relationship between the debris and the splat sizes in the mild wear of the conventional coating. A similar result can be found for the modified coating mild wear because the mean debris size is correlated with the interparticle spacing between PM zones. Under severe wear conditions, no link between the debris size and microstructural features can be confirmed.

5. Conclusions

Mechanical and tribological characterization has been carried out on Al_2O_3 –13% TiO_2 conventional and modified coatings that were deposited by atmospheric plasma spray. The following conclusions were drawn:

A statistical analysis of the Young's modulus, hardness and fracture toughness data were performed. Independent of the mechanical properties, the modified coating is assumed to behave as a composite material. The properties of each constituent (PM and FM domains) were determined by depth-sensing indentation, and the effective properties of the coatings were obtained via a rule of mixtures.

An energetic approach, developed through dimensional analysis, has been used to explain wear data. The wear rate, put in terms of the wear coefficient, kH , has been expressed as a function of a dimensionless parameter that comprises a form of the input energy to the tribosystem and a form of the energy dissipated by the material during the wear process. The input energy can be expressed as the product of the friction coefficient, the normalized normal pressure and the normalized sliding velocity. The key to this methodology is the fact that the dissipated energy depends upon the operation wear mechanism. When the main wear mechanism is brittle crack propagation, the dissipated energy can be written as a dimensionless function of the energy-release rate, G . If the wear coefficient is represented in relation to the dimensionless contact severity parameter, ($\frac{\mu P_T}{G}$), the wear data that correspond to both coatings can be described by the same function.

The multiphase character of the modified coating was described through its effective Young's modulus, hardness and fracture toughness. We propose that the global wear behaviour of a material is governed by its global or effective properties. The materials studied in this work, conventional and modified, have the same composition but different microstructural features; consequently, they have different effective properties. Their wear behaviour is clearly different, but it can be described by the same equation because dimensionless parameters were used and the same wear mechanism was observed in both cases. The different behaviour was determined through the effective mechanical properties of each coating.

Acknowledgements

The authors are indebted to Comunidad de Madrid for its financial support through the ESTRUMAT program. Thanks are also extended to Dr. A. Salazar for her help during the manuscript revision.

References

- [1] Ananthapadmanabhan PV, Thiyagarajan TK, Satpute RU, Venkatramani N, Ramachandran K. Surf Coat Technol 2003;168:231–40.
- [2] Ramachandran K, Selvarajan V, Ananthapadmanabhan PV, Sreekumar KP. Thin Solid Films 1998;315:144–52.
- [3] Erickson LC, Hawthorne HM, Troczynski T. Wear 2001;250:569–75.
- [4] Pantelis DI, Psyllaki P, Alexopoulos N. Wear 2000;237:197–204.
- [5] Gessasma S, Bounazef M, Nardin P, Sahraoui T. Ceram Int 2006;32:13–9.
- [6] Normand B, Fervel V, Coddet C, Nikitine V. Surf Coat Technol 2000;123:278–87.
- [7] Shaw LL, Goberman D, Ren R, Gell M, Jiang S, Wang Y, et al. Surf Coat Technol 2000;130:1–8.
- [8] Wang Y, Jiang S, Wang M, Wang S, Xiao TD, Strutt PR. Wear 2000;237:176–85.
- [9] Gell M, Jordan EH, Sohn YH, Shaw L, Xiao TD. Surf Coat Technol 2001;146–147:48–54.
- [10] Jordan EH, Gell M, Sohn YH, Goberman D, Shaw L, Jiang S, et al. Mater Sci Eng 2001;A301:80–9.
- [11] Goberman D, Sohn YH, Shaw L, Jordan E, Gell. Acta Mater 2002;50:1141–52.
- [12] Liu Y, Fischer ET, Dent A. Surf Coat Technol 2003;167:68–76.
- [13] Bansal P, Padture NP, Vasiliev A. Acta Mater 2003;51:2959–70.
- [14] Lin X, Zeng Y, Lee SW, Ding C. J Eur Ceram Soc 2004;24:627–34.
- [15] Cao XQ, Vassen R, Schwartz S, Jungen W, Tietz F, Stöver D. J Eur Ceram Soc 2000;20:2433–9.
- [16] Rodriguez J, Rico A, Otero E, Rainforth WM. Acta Mater 2009;57:3148–56.
- [17] Rico A, Rodriguez J, Otero E, Zeng P, Rainforth WM. Wear 2009;267:1191–7.
- [18] Rico A. PhD dissertation, Universidad Rey Juan Carlos, Madrid; 2009.
- [19] Adachi K, Kato K, Chen N. Wear 1997;203–204:291–301.
- [20] Hsu SM, Wang YS, Munro RG. Wear 1989;134:1–11.
- [21] Kato K. In: Proceedings of the international tribology conference; 1995. p. 421–6.
- [22] Hokkirigawa K, Kato K. In: Proceedings of the 33rd JSLE conference; 1989. p. 9–12.
- [23] Wang YS, Hsu SM, Munro RG. Lubri Eng STLE 1991;47(1):63–9.
- [24] Lee SW, Hsu SM, Shen MC. J Am Ceram Soc 1993;76(8):1937–47.
- [25] Blomberg A, Olsson M, Hogmark S. Wear 1994;171:77–89.

- [26] Dong X, Jahanmir S, Hsu SM. *J Am Ceram Soc* 1991;74 5:1036–44.
- [27] Dong X, Jahanmir S. *Wear* 1993;165:169–80.
- [28] Akazawa M. In: Proceedings of the international congress on tribology—5th Eurotrib'89; 1989. p. 126–31.
- [29] Hokkirigawa K, Kato K, Araya S. In: Proceedings of the Japan international tribology conference; 1990. p. 1425–30.
- [30] Xu J, Kato K. In: Proceedings of the international symposium on microsystems, intelligent materials and robots; 1995. p. 122–5.
- [31] Chen N, Adachi K, Kato K. *Trans JSME C* 61 1995;584: 1605–12.
- [32] Lim SC, Ashby MF. *Acta Metall* 1987;35(1):1–24.
- [33] Antoniou R, Subrananian C. *Scripta Metall* 1989;22:80–3.
- [34] Childs T.H. In: Proceedings of the institution of mechanical engineers, vol. 20(2); 1988. p. 379–95 (C6).
- [35] Briscoe BJ, Evans PD. In: Proceedings of the wear of materials; 1989. p. 449–57.
- [36] Kato K, Hokkirigawa K. In: Proceedings of the international congress of Tribology—Eurotrib'85; 1985. p. 1–5.
- [37] Hsu SM, Shen M. *Wear* 2004;256:867–78.
- [38] Oliver WC, Pharr GM. *J Mater Res* 1992;7:1564–83.
- [39] Anstis GR, Chantikul P, Lawn BR, Marshall DB. *J Am Ceram Soc* 1981;64:533–8.
- [40] Li X, Diao D, Bushan B. *Acta Mater* 1997;44:4453–61.
- [41] ASTM G99-04. Standard test method for wear testing with a pin on disk apparatus; 1999.
- [42] Rose LRF. *Mech Mater* 1987;6:11.
- [43] Bower AF, Ortiz M. *J Mech Phys Solids* 1991;39:815.
- [44] Williams JA. *Tribol Int* 2005;28:863–70.
- [45] Buckingham E. *Phys Rev* 1914;4:345–76.